Cloud-Resolving Model Simulations and a Simple Model of an Idealized Walker Cell

JONATHAN WOFSY AND ZHIMING KUANG

Department of Earth and Planetary Sciences, Harvard University, Cambridge, Massachusetts

(Manuscript received 28 November 2011, in final form 8 May 2012)

ABSTRACT

An idealized Walker cell with prescribed sea surface temperature (SST) and prescribed radiative cooling is studied using both a two-dimensional cloud-resolving model (CRM) and a simple conceptual model. In the CRM, for the same SST distribution, the width of the warm pool (area of strong precipitation) varies systematically with the magnitude of the radiative cooling, narrowing as radiative cooling is increased. The simple model is constructed to interpret these behaviors. Key aspects of the simple model include a surface wind determined from the boundary layer momentum budget, which in turn sets evaporation assuming a spatially uniform surface relative humidity, prescribed gross moist and dry stratification as a function of column water vapor and precipitation, and a gustiness enhancement on evaporation in areas of precipitation. It is found that the gustiness enhancement, likely due to mesoscale systems, creates a feedback that narrows the warm pool. This process has not been included in previous formulations of the simple model and its role is emphasized here.

1. Introduction

The tropical atmospheric circulation is a major component of the climate system, characterized by complex coupling between large-scale flows and small-scale processes such as moist convection. Changes in the tropical atmospheric circulation and associated clouds are important contributors to Earth's climate sensitivity (Bony et al. 2006). It is our goal to better understand the tropical circulation.

The framework adopted here involves studying a prototype tropical climate system using two numerical models of differing complexity, one being a cloud-resolving model (CRM) and the other a simple theoretical model. We simulate an idealized Walker cell: the equatorial overturning circulation characterized by ascent, deep atmospheric convection, and high precipitation over the west Pacific warm pool, and descent, a temperature inversion capping a turbulent boundary layer, and low precipitation over the east Pacific cold pool. The Walker cell is important in the overall climatology of the tropics and El Niño. Idealized Walker cells are more amenable to cloud-resolving simulations (simulations that, instead of using convective parameterizations, explicitly simulate convective-scale motions) than more realistic circulations of the entire tropics. At the same time, they also contain the main types of moist convection and serve as a good prototype problem, capable of probing the complex interactions involved with climate feedbacks. Insights gained here on the coupling between the large-scale and small-scale processes can then be applied to better understand the tropical circulation in its full complexity.

In addition to state-of-the-art models, a wide variety of simple models have been used to study the Walker cell. The philosophy behind constructing a simple model is to reduce a physical system to its essential physical mechanisms, which furthers understanding by showing how the modeled phenomena affect or contribute to the full system. Some of the most simplistic models of the Walker cell have involved two boxes, with a warm pool in one box and a cold pool in the other. These models have been used to examine a wide range of phenomena associated with the tropics. For instance, Pierrehumbert (1995) developed a model that looked at the heat balance between the two pools, emphasizing the role of the cold pool's ability to radiate longwave radiation to space as a mechanism for maintaining tropical sea surface temperature (SST). Larson et al. (1999) examined how

Corresponding author address: Jonathan Wofsy, Department of Earth and Planetary Sciences, Harvard University, Cambridge, MA 02138.
E-mail: jwofsy@post.harvard.edu

DOI: 10.1175/JCLI-D-11-00692.1

moisture, temperature, clouds, and boundary layer height changed as the size of the boxes were varied and radiative forcing was increased. Kelly and Randall (2001) made a similar model, but predicted the pool widths and included a sloping boundary layer in the cold pool. This list of two box models is not meant to be exhaustive; rather, it highlights the wide range of phenomena that have been studied with simple models.

Another simple model, known as the Simplified Quasi-Equilibrium Tropical Circulation Model (SQTCM), was described in Bretherton and Sobel (2002) and Peters and Bretherton (2005, hereafter PB05). It was a one-dimensional model of the Walker cell, with a single dimension along the equator, combining quasi-equilibrium theory (Arakawa and Schubert 1974; Emanuel et al. 1994) with the weak temperature gradient approximation (WTG) (Sobel and Bretherton 2000; Sobel et al. 2001). Quasi-equilibrium implies that tropical temperature profiles remain close to a moist adiabat. WTG states that horizontal differences in temperature are small in the tropical atmosphere. Combining these two simplifications with a moist static energy (MSE) budget, gross moist stability (GMS) calculation, and a simple convective parameterization, PB05 constructed a one-dimensional model of the Walker cell where all columns were vertically integrated. We have chosen to modify the model of PB05 for use in this study.

Studies using medium complexity models such as the Quasi-Equilibrium Tropical Circulation Model (QTCM) (Neelin and Zeng 2000) and high complexity models such as global circulation models (e.g., Wyant et al. 2006) have been partially successful in recreating observed tropical climate, but large biases remain (e.g., Bretherton 2007). Even these more complex simulations rely on parameterizations of moist convection, which operates on much smaller scales than the resolution of the models.

The most realistic numerical models currently available for simulating tropical circulations are CRMs. When run at high horizontal resolution ($\sim$1 km) over a domain on the order of the Walker cell ($\sim$10 000 km), they can simulate the coupling of small-scale turbulence of convection to the large-scale circulation. The increase in realism comes with the cost of a high computational burden, limiting the domain size for such simulations. The Walker cell's natural two-dimensional geometry makes it a good choice for simulation in a CRM. Previous studies of the Walker cell in a CRM were forced by a SST gradient on a two- or three-dimensional "bowling alley" domain (Grabowski et al. 2000; Bretherton 2007; Liu and Moncrieff 2008). We will be using a similar setup in our CRM simulations.

A useful strategy to improve our understanding of the Walker cell is to compare results from a simple model and a CRM in the same setting. Bretherton et al. (2006) pioneered such an approach and compared CRM simulations to SQTCM results as a way to verify the simple model. They compared the broad circulation features and the MSE budgets of the models as a means of examining changes in warm pool width when SSTs were changed.

In this work, we draw inspiration from Bretherton et al. (2006) and also compare CRM simulations to a simple theoretical model, but in more detail. We use a more simplified setup, with fixed radiative cooling in the troposphere in addition to fixed SSTs, eliminating radiative feedbacks. We use domains that are sufficiently large to eliminate the somewhat artificial gravity wave resonance that gave rise to the strong eddy activity in Bretherton et al. (2006). While we have attempted more comprehensive simulations of the Walker cell in the CRM with a range of domain sizes, radiative feedbacks, and a mixed layer ocean, the results had highly variable, nonlinear behavior, a result echoing that of Bretherton (2007). This motivated the simplified setup used in this study. We felt that a clearer understanding of the simpler system was needed before including additional processes. The simple model is based on that of PB05 but takes more direct guidance from the CRM. From diagnosing the CRM, we find that wind gusts can enhance the surface latent heat flux (LHF; also called evaporation) in areas of precipitation. The gustiness enhancement of surface heat fluxes due to mesoscale convective systems has been found in CRMs modeling the tropics (e.g., Jabouille et al. 1996) and in observations of the tropical Pacific ocean (e.g., Esbensen and McPhaden 1996). The inclusion of gustiness in our simple model creates a feedback mechanism that is capable of narrowing the warm pool when radiative cooling is increased. We feel this result makes a case for the inclusion of gustiness in simpler models that parameterize moist convection. We also change the calculation of gross moist and dry stratification to better capture the CRM behavior.

The outline of the paper is as follows: In section 2 we introduce the CRM and show results from simulations. In section 3 we present the simple model and detail changes made relative to PB05. In section 4 we present results from the simple model and compare them to results from the CRM, detailing important mechanisms in the model. In section 5 we discuss our results and present our conclusions.

2. Cloud-resolving model results

a. Control results

In this subsection we present the setup and illustrative fields for the control case CRM simulation.

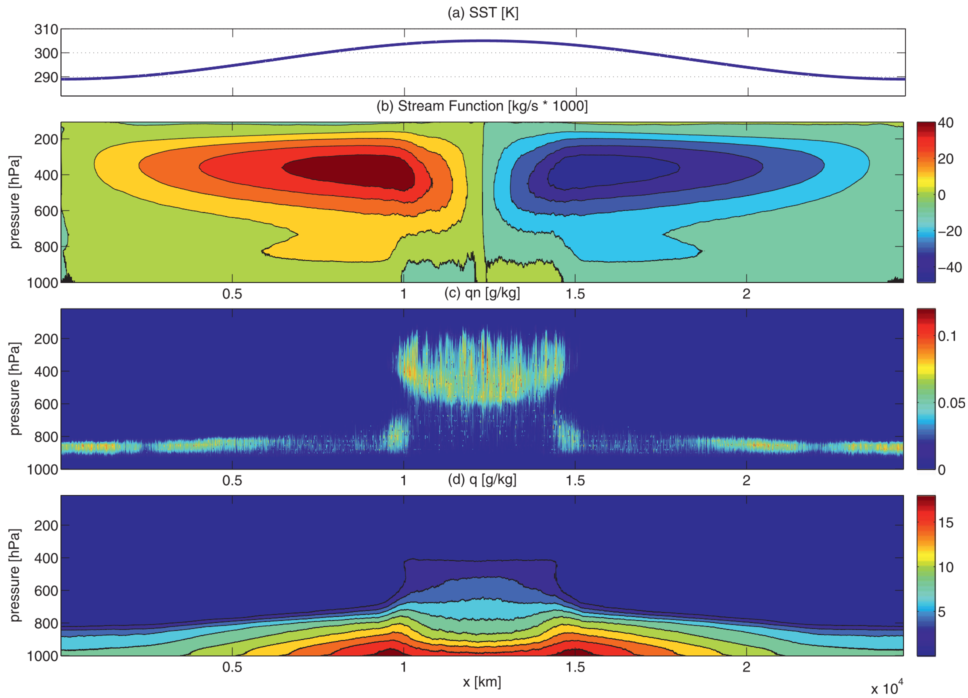

FIG. 1. (a) SST distribution for all model runs, and CRM control run results for (b) streamfunction, (c) cloud condensates, and (d) water vapor.

The CRM we use is version 6.6 of the System for Atmospheric Modeling, which is an anelastic nonhydrostatic model with bulk microphysics that by definition uses no cumulus parameterization. A simple Smagorinsky-type scheme is used to represent the effect of subgrid-scale turbulence. The surface fluxes of sensible heat, latent heat, and momentum are computed using the Monin–Obukhov similarity theory. Our domain is two-dimensional. There are 64 vertical levels with variable spacing as fine as 75 m near the surface, coarsening with height. The model has a rigid lid just above 26 km with a wave-absorbing layer occupying the upper third of the domain to prevent the reflection of gravity waves. Horizontal resolution is 2 km, aligned along the equator. Periodic lateral boundary conditions are employed. A fixed radiative cooling rate of 1.3 K day^{-1} is imposed in the troposphere with Newtonian damping in the stratosphere (Pauluis and Garner 2006). SSTs are fixed with the form

$$\mathrm{SST}(x) = \mathrm{SST}_0 - \Delta\mathrm{SST}\cos\left(\frac{2\pi x}{A}\right), \tag{1}$$

where A is the domain width set to 24 576 km, creating a maximum SST at the midpoint of the domain. Here, SST_0 is set to 297 K and ΔSST is 8 K. A plot of SST is shown in Fig. 1a. With fixed SSTs and radiative cooling, radiative feedbacks are eliminated, simplifying the system. The model is run for 200 days and reaches equilibrium after approximately 50 days. Averaged fields from the CRM are computed from the last 100 days of model output. A full description of the model formulation and equations is given in Khairoutdinov and Randall (2003), to which the reader is referred for more details.

This setup produces an overturning, Walker-like circulation with ascent over the warm pool and descent over the cold pool that can be seen in the plot of mass streamfunction (Fig. 1b). Here, the warm pool is defined as the area where $P > \overline{P}$, where P is precipitation and the domain-mean precipitation is $\overline{P}$ (where a bar over a variable denotes an average over the domain). The cold pool is defined as the area where $P \leq \overline{P}$. The warm pool in this simulation spans roughly from x = 9500 km to x = 15 000 km, with the cold pool encompassing the rest of the domain. While the SSTs are fixed, the size of the warm pool and cold pool as we have defined them can change if precipitation changes. Another structure seen in the circulation is a shallow (below 800 mb) reverse circulation over the warm pool. This is presumably driven by evaporation of rain, with such divergence commonly observed in mesoscale convective systems (Mapes and Houze 1995). This is a different structure from the multicell structures seen in previous simulations of Walker cells in CRMs (e.g., Grabowski et al. 2000), which were due to radiative cooling profiles that

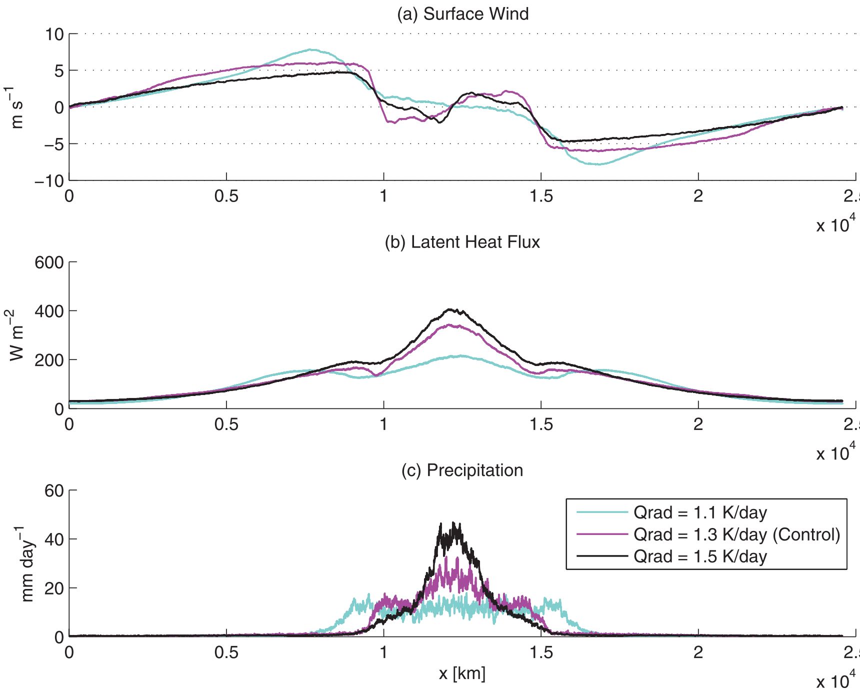

FIG. 2. The 1D CRM fields for different radiative cooling rates (denoted by Qrad): (a) surface winds, (b) latent heat flux, and (c) precipitation.

deviated from the first baroclinic mode. Such cells are eliminated by the fixed radiative cooling rate that we use. The cloud condensates field, presented in Fig. 1c, shows a shallow, dense cloud layer below 800 hPa over the cold pool, which occurs in the boundary layer. On the edge of the warm pool, shallow convection occurs in a thin band with thick clouds in the lower troposphere, giving way to deep convection and cumulus towers that reach the tropopause in the center of the warm pool. The boundary layer is capped by a temperature inversion and distinguished by high water vapor content, visible in the humidity field shown in Fig. 1d. Areas of deep convection over the warm pool are characterized by an increase water vapor above the boundary layer (above ~800 hPa). This bears a resemblance to the observed Walker cell.

In Fig. 2 we present the steady-state fields of surface winds, LHF, and precipitation to provide further details of the control results. Additionally, their one-dimensionality facilitates comparison with our simple model, which we do in section 4. Surface winds (Fig. 2a, magenta line) increase in the cold pool when moving toward the warm pool, driven by the underlying SST gradient, before slacking over the warm pool where convection occurs. LHF (Fig. 2b, magenta line) increases in a similar manner to surface winds over the cold pool, but peaks over the warm pool in an area of low mean surface winds. This is due to an enhancement associated with surface wind gustiness and will be discussed in more detail in later sections. Sensible heat flux is much smaller than LHF and is not presented. Precipitation (Fig. 2c, magenta line) is light over the cold pool, and begins abruptly in the warm pool, peaking over the warmest SST.

b. *Response to variable radiative cooling rates*

We expand the scope of the study by examining how the Walker cell responds to changes in forcing, with the hope that the results will be easy to interpret given our simplified setup. Here we choose to vary radiative cooling rates. Since SSTs are not changed, this experiment can be thought of as a partial derivative to a change in CO_2, with a decrease in radiative cooling rate corresponding to an increase in CO_2. We run an increased radiative cooling rate case of 1.5 K day^{-1} and a decreased radiative cooling rate case of 1.1 K day^{-1}. The intermediate cases of 1.2 and 1.4 K day^{-1} have also been run, with the 1.2 K day^{-1} displaying a monotonic change and 1.4 K day^{-1} being close to that of the 1.5 K day^{-1}. We therefore present only the end members. This change in radiative cooling represents a very large change in CO_2, but that is to more easily see the response. More extreme cases have also been run and will be briefly discussed in later sections. We use the current subsection to show the behavior of the CRM and present the explanations for the behavior in section 4.

The intuitive effect of increasing radiative cooling is an increase in domain-averaged latent heating to maintain energy balance (ignoring small changes in sensible heat flux). While this effect is present (Fig. 2b), it is nonuniform in space, with most of the increase taking place over the warm pool.

The steady-state circulation strength increases with increased radiative cooling. This can be understood from the cold pool radiative balance in the absence of temperature changes and horizontal advection:

$$\omega = \frac{Q}{\frac{\partial \theta}{\partial p}}.$$

Here ω is pressure velocity, Q is radiative heating (negative of radiative cooling), θ is potential temperature, and p is pressure, with $\partial\theta/\partial p$ being the stratification. Stratification does not change much as the temperatures closely follow a moist adiabat and SSTs are fixed to be the same in all cases. Therefore, increased subsidence is needed to balance the increase in radiative cooling. Since the cold pool area is large in all cases, this larger subsidence rate will drive a stronger circulation. An increased circulation strength, however, does not require that the surface winds increase, since the boundary layer is somewhat decoupled from the overlying atmosphere in these experiments. Surface winds (Fig. 2a) slightly decrease when radiative cooling is increased, showing that circulation strength is not a good indicator of low-level winds. Furthermore, all three cases have very low surface winds over the warm pool. The control on surface winds is important because it affects surface heat fluxes, boundary layer depth, precipitation, and possibly cloud albedo, as remarked upon in Nuijens and Stevens (2012).

With sensible heat flux being small, domain averaged LHF must be approximately equal to radiative cooling, which must in turn be approximately equal to domain averaged precipitation. Precipitation therefore increases with increasing radiative cooling rate and, notably, it increases preferentially over the warmest SST, accompanied by a distinct narrowing of the warm pool (Fig. 2c), by ~2000 km from 1.1 to 1.3 K day^{-1} and an additional ~400 km from 1.3 to 1.5 K day^{-1}.

3. Simple model formulation

a. A previous simple model

In an attempt to explain the behavior of the CRM simulations, we turn to the simple model of PB05, the ideology being that a simple model can illuminate relevant aspects of the complex model by parameterizing the key physics through simplified equations. The PB05 model has one spatial dimension aligned along the equator. It was made with the purpose of exploring various tropical feedbacks. The model equations are presented in the next subsection. For a complete model overview, interested readers are referred to PB05.

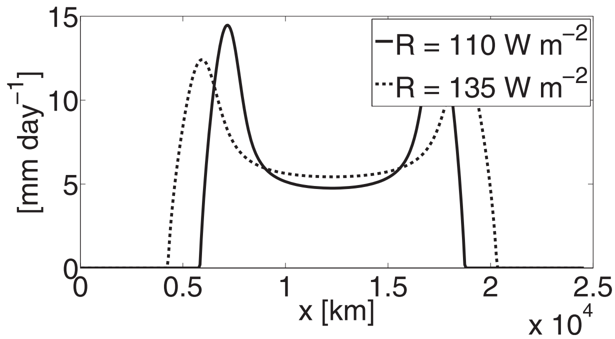

FIG. 3. Precipitation for runs with radiative cooling rates of 110 (solid) and 135 W m^{-2} (dashed) using the original formulation of the PB05 model.

When we ran the model with the same setup as the CRM and forced it by changing radiative cooling rates, it produced the qualitatively *opposite* result, with the warm pool widening (instead of narrowing) when radiative cooling was increased (Fig. 3). This result is not in contrast to the warm pool behavior seen in Bretherton et al. (2006), where they found a narrowing warm pool when SST was uniformly raised and attributed it to a decrease in gross moist stability. The qualitative disagreement between the CRM and PB05 in the current setting points to the need for improvements in the simple model, which motivates us to further develop the simple model with more direct guidance from the CRM.

b. Model equations

The basic equations of our model are based on PB05 and are presented below. They are altered to allow for horizontal variability in the vertical profiles of velocity. Many of the parameterizations employed by our model have been modified from PB05 and are discussed in the subsections to follow.

The model of PB05 and our model are built off of the QTCM, which assumes strict quasi-equilibrium such that the effects of moist convection keep the temperature profile close to a moist adiabat. In PB05, the QTCM was further simplified with WTG, as it is here. Model variables are computed as a perturbation from a constant reference state, which is denoted with a subscript zero. In PB05 and the QTCM, perturbations are in the form of a fixed unitless vertical structure dependent on pressure p multiplied by an amplitude that depends on the time t and horizontal location x. However, observations indicate that the vertical structures of the velocity field are not horizontally uniform (e.g., Back and Bretherton 2006; Peters et al. 2008). As we will show, this is also the case for our CRM simulations. Therefore, we allow the vertical structures of the velocity field to vary in the horizontal. Also, we allow for spatial variations in moisture fields to capture a boundary layer with constant relative humidity and temperature equal the underlying SST. We introduce the model variables in Eqs. (2)–(5). Temperature T is defined as

$$T(p,t) = T_0(p) + a(p)T_1(t), \tag{2}$$

which has no horizontal variability in the WTG framework. This equation is unaltered from PB05. The decomposition of moisture q is

$$q(x,p,t) = q_0(x) + b(p)q_1(x,t) + c(p)q_2(x), \tag{3}$$

where the addition of the $c(p)q_2(x)$ term differs from PB05. The quantity q_2 is the boundary layer moisture assuming that relative humidity is fixed in the boundary layer and the temperature in the boundary layer is that of the underlying ocean, and q_1 is the free tropospheric moisture from PB05. Boundary layer moisture and free tropospheric moisture have somewhat different roles in dynamics: the boundary layer moisture plays a major role in determining surface latent heat flux through relative humidity and also in the amount of convective available potential energy of the column. The free tropospheric moisture is important in modulating the shape of moist convection (Brown and Zhang 1997; Parsons et al. 2000; Derbyshire et al. 2004; Kuang and Bretherton 2006; Peters et al. 2008). To further illustrate this point, we compare control run values of the CRM vertically integrated moisture, or water vapor path (WVP) (Fig. 4), of the full column (solid) and areas above 2000 m (dashed), representing the free troposphere. The free troposphere is mostly dry until a spike over the warm pool corresponding to a rapid rise in precipitation compared to the cold pool (Fig. 2c). In contrast, the full column shows a decrease in WVP over the warm pool, associated with a reduction in boundary layer moisture, demonstrating the need for separation between the boundary layer and free tropospheric moisture. Such a separation was also suggested by Holloway and Neelin (2009) using radiosonde data. This is done by viewing the moisture field we model as the column moisture minus a spatially varying but time-constant boundary layer moisture field that is fixed at the outset and does not participate in the adjustment by advection, diffusion, or precipitation. Therefore, we specify that $c(p)$ is

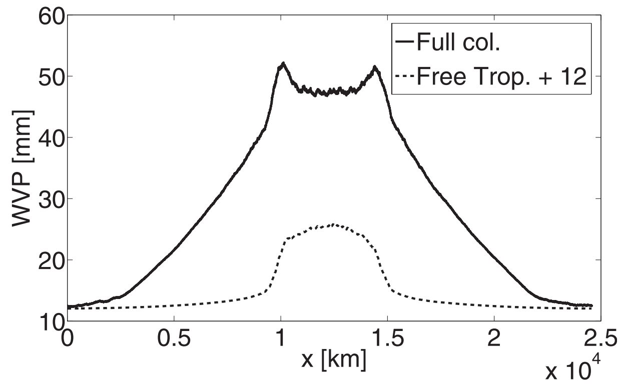

FIG. 4. The WVP from the total column (solid) and the free troposphere (dashed). Free tropospheric values have a constant value of 12 mm added for ease in comparison.

a structure function that is nonzero only in the boundary layer and $b(p)$ is a structure function that is nonzero only in the free troposphere above the boundary layer. This is done as a minimalistic approach to capture moisture variations with a single prognostic variable.

Horizontal winds u and pressure velocity ω, are defined by

$$u(x,p,t) = V(x,p)u_1(x,t), \tag{4}$$

$$\omega(x,p,t) = \Omega(x,p)\omega_1(x,t), \tag{5}$$

where both V and Ω now have x dependence. Thermodynamic variables (q and T) are expressed in equivalent energy units (J kg^{-1}).

The domain length is half of that used in the CRM and the boundary conditions are wall-like at the domain edges with $u(0) = u(A/2) = 0$. SSTs are fixed using Eq. (1) with the same SST gradient. The model equations are Eqs. (6) and (9)–(11). They are solved over the domain $0 \le x \le A/2$ and one-dimensionalized by integrating variables through the troposphere. We begin with the PB05 continuity equation, following their sign convention:

$$\frac{\omega_1}{\Delta p_T} = \frac{\partial u_1}{\partial x}. \tag{6}$$

We now derive the equations for T_1 and q_1 as follows. Let us start with the vertically integrated moisture equation:

$$\frac{1}{g}\frac{\partial}{\partial t}\int_{p_T}^{p_s} q\,dp + \frac{1}{g}\frac{\partial}{\partial x}\int_{p_T}^{p_s} uq\,dp - \frac{1}{g}\int_{p_T}^{p_s} \nabla\cdot(\kappa\nabla q)\,dp = E - P,$$

where our diffusion coefficient κ varies with height. Using Eq. (4) and noting that u_1 is not a function of p, we have

$$\frac{1}{g}\frac{\partial}{\partial t}\int_{p_T}^{p_S} q\,dp + \frac{1}{g}\frac{\partial}{\partial x}\left(u_1\int_{p_T}^{p_S} Vq\,dp\right) - \frac{1}{g}\int_{p_T}^{p_S}\nabla\cdot(\kappa\nabla q)\,dp = E - P.$$

Similarly, the vertically integrated temperature equation is

$$\frac{1}{g}\frac{\partial}{\partial t}\int_{p_T}^{p_S} T\,dp + \frac{1}{g}\frac{\partial}{\partial x}\left(u_1\int_{p_T}^{p_S} Vs\,dp\right) = P - R,$$

where $s = C_pT + gz$ is the dry static energy, E is evaporation, P is precipitation, and R is net atmospheric radiative cooling. Sensible heat is neglected. Using Eqs. (4) and (6) and the following definitions,

$$\hat{a} \equiv \frac{1}{\Delta p_T}\int_{p_T}^{p_S} a\,dp,$$

$$\hat{b} \equiv \frac{1}{\Delta p_T}\int_{p_T}^{p_S} b\,dp,$$

$$\hat{\kappa} \equiv \frac{1}{\Delta p_T}\int_{p_T}^{p_S} \kappa b\,dp,$$

$$M_s(t) \equiv \frac{-1}{\Delta p_T}\int_{p_T}^{p_s} V(x,p)s(p,t)\,dp, \qquad (7)$$

$$M_q(x,t) \equiv \frac{1}{\Delta p_T}\int_{p_T}^{p_s} V(x,p)q(x,p,t)\,dp, \qquad (8)$$

we arrive at our integrated temperature and moisture equations:

$$\frac{\Delta p_T}{g}\left[\hat{a}\frac{\partial T_1}{\partial t} - \frac{\partial(u_1M_s)}{\partial x}\right] = P - R, \qquad (9)$$

$$\frac{\Delta p_T}{g}\left[\hat{b}\frac{\partial q_1}{\partial t} + \frac{\partial(u_1M_q)}{\partial x} - \nabla\cdot(\hat{\kappa}\nabla q_1)\right] = E - P. \qquad (10)$$

These are closely related to the QTCM temperature and moisture equations. For the moisture equation, we assume that $\kappa(p)$ is nonzero only in the free troposphere. We do not consider diffusion in the boundary layer as boundary layer moisture is assumed to be constant in time and of a fixed form. Moisture diffusion was not included in PB05. It is added here mainly to obtain smoother solutions and can be thought of as representing horizontal eddy advection. The quantity M_q depends on q_2, so q_2 enters the model through Eq. (10). Also, Δp_T is the tropospheric pressure thickness and $\Delta p_T = p_S - p_T$, where p_S is surface pressure and p_T is the tropopause pressure; M_q and M_s are the gross moisture and dry static energy stratification. We demand that M_s has no x dependence so that

$$\int_{p_T}^{p_S} V(x,p)s(p)\,dp = \text{horizontally invariant constant},$$

when time dependence is ignored. This removes some of the ambiguity from the decomposition in Eq. (4) and has no effect on model results other than changing the values of u_1 and ω_1.

The final model equation is

$$\hat{a}\frac{\Delta p_T}{g}\frac{\partial T_1}{\partial t} = \frac{2}{A}\int_0^{A/2}(P - R)\,dx, \qquad (11)$$

which is a domain integration of Eq. (9). It is used to calculate T_1. The order of solving is as follows: first, Eq. (10) is used to solve for q_1, followed by Eq. (11), then Eq. (9) is used next to calculate ω_1, and finally Eq. (6) is used to calculate u_1. They are solved until a steady state is reached. We note that the temperature equation is not of sufficient order of accuracy to satisfy momentum balance in the free troposphere. In the spirit of WTG, free tropospheric momentum balance is not included in the model, but could be used to solve for the temperature structure beyond what is retained here, after the velocity field is obtained (Sobel and Bretherton 2000).

The precipitation parameterization is Betts–Miller-like (Betts and Miller 1986) with

$$P = \max\left(\frac{\Delta p_T}{g}\frac{q_1 - T_1}{\tau_c} + P_0, 0\right), \qquad (12)$$

which is unaltered from PB05.

Parameter choices are listed in Table 1. In the next subsections we discuss our modifications to the model.

TABLE 1. Simple model parameter values.

Parameter	Symbol	Value
Tropospheric pressure depth	Δp_T	900 hPa
Vertical average of a	$\hat{a}$	0.459
Vertical average of b	$\hat{b}$	0.316
Vertical average of diffusion coefficient	$\hat{\kappa}$	500 000 m^2 s^{-1}
Convective adjustment time scale	τ_c	48 h
Gross dry static energy stratification	M_s	2860 J kg^{-1}
Drag feedback	K_{c_d}	145 W m^{-2}
Bulk scheme constant	c_q	0.009
Background wind speed	u_0	2 m s^{-2}
Gustiness factor	K_p	0.0054 (m s^{-1})^2 (W m^{-2})$^{-(3/2)}$

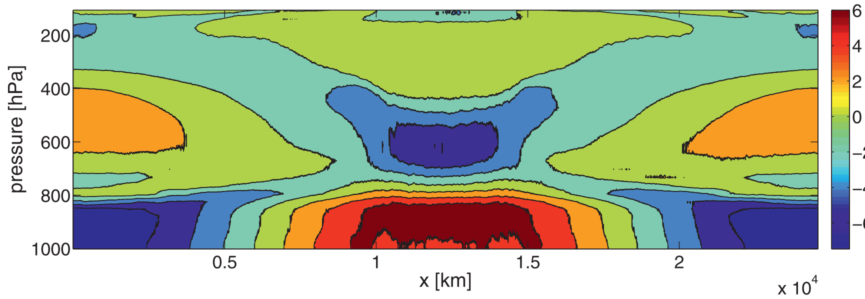

FIG. 5. Deviation from layer mean temperature (°C) for the CRM control run.

c. Surface wind calculation

While the WTG framework is a good approximation for modeling the tropical free troposphere, it does not capture the behavior of the boundary layer, where, because of high friction, large temperature gradients can exist (Fig. 5). In PB05, surface winds were not calculated or used in computing surface fluxes. Here, we calculate surface winds by solving the steady-state momentum equation of the boundary layer, in the same spirit as Lindzen and Nigam (1987):

$$u_b\frac{\partial u_b}{\partial x} = -\frac{1}{\rho_0}\frac{\partial p_b}{\partial x} - \frac{c_d}{H}u_b^2, \qquad (13)$$

where u_b is the boundary layer wind, H is the boundary layer height, c_d is the drag coefficient, p_b is the pressure integrated through the boundary layer, and ρ_0 is the density of the boundary layer air, assumed to be uniform. Vertical momentum flux across the boundary layer top is neglected. The pressure gradient at the top of the boundary layer is small in the CRM simulations, and therefore ignored. Thus, the boundary layer pressure gradient can be calculated from the boundary layer temperature gradient using the hydrostatic equation. Through these assumptions, Eq. (13) can be recast as follows:

$$\frac{1}{2}\frac{\partial u_b^2}{\partial x} = \frac{gH}{\mathrm{SST}_0}\frac{2\pi}{A}\Delta\mathrm{SST}\,\sin\left(\frac{2\pi x}{A}\right) - \frac{c_d}{H}u_b^2. \qquad (14)$$

A full derivation of our boundary layer wind solution is presented in an appendix. To calculate the surface wind, u_s, u_b is scaled by a constant factor $\alpha = 0.70$ to approximate the effects of friction immediately above the surface, such that $u_s = \alpha u_b$. The boundary layer thickens toward the warm pool as subsidence in the free troposphere decreases, so we approximate H as having a linear slope with the form

$$H = m_b x + H_{\min}. \qquad (15)$$

Over the cold pool, this height roughly coincides with the trade inversion. Over the warm pool, where there is no trade wind inversion, defining the boundary layer height is not as straightforward. Rather than having a separate treatment of boundary layer height over the warm pool, we apply Eq. (15) over the whole domain and parameterize warm pool effects on the boundary layer momentum budget, as will be discussed momentarily. In our simple model, the boundary layer slope is set so the total change in boundary layer height is 1200 m and height of the boundary layer top over the coldest SST, $H_{\min}$, is set to 850 m. These heights are roughly estimated from the CRM by finding the heights of maximum dq/dz over the cold pool (Fig. 1d). Equation (14) can now be solved and the simple model surface winds can be compared to the CRM surface winds. When calculated, the simple model surface winds (Fig. 6, green) are similar to the CRM surface winds (blue) over the cold pool, but do not decelerate fast enough over the warm pool. In the CRM, the warm pool is an area of deep convection and momentum is being mixed through a much deeper column, slowing the winds. We parameterize this effect by increasing drag in areas of precipitation as follows:

$$c_d = c_{d_0}\left(1 + \frac{P}{K_{c_d}}\right), \qquad (16)$$

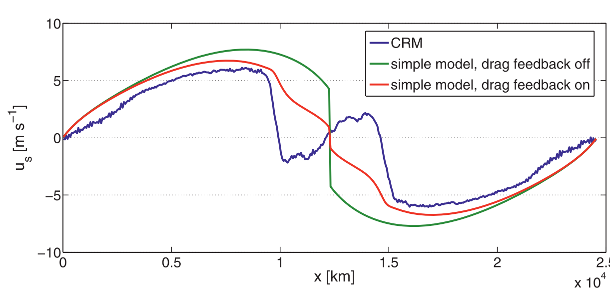

FIG. 6. Surface winds from CRM control run (blue), simple model without the precipitation-drag feedback (green), and simple model with the precipitation-drag feedback (red).

with c_{d_0}, the cold pool drag, set to 0.0013. The term K_{c_d} is a constant representing the strength of precipitation-drag feedback with units W m^{-2}. Its magnitude is tuned to give a reasonably sized warm pool in the simple model. The slowing winds could also be captured by increasing H in the warm pool. In a full run of the simple model, this feedback helps produce a surface wind (Fig. 6, red) that has better qualitative agreement with the CRM over the warm pool.

It should be noted that the boundary layer is considered to be sufficiently thin that any ω generated from boundary layer convergence is negligible. In the CRM control run, the average ω over the warm pool (spanning approximately $x = 9500$ km to $x = 15\,000$ km) at a height of 2 km is about 20% of the maximum average ω over the warm pool, which occurs near $z = 8$ km.

d. *Evaporative flux parameterization*

In PB05, the evaporative flux was approximated by a bulk scheme that relied only on relative humidity computed using the column integrated moisture. We have changed the LHF parameterization to be a function of surface wind speed and included the effect of transient wind gusts with the following bulk scheme:

$$E = c_q(1 - \mathrm{RH})q_s^\star\sqrt{u_s^2 + u_0^2 + K_pP^{3/2}}, \qquad (17)$$

where c_q is a constant, RH is the relative humidity at the surface, $q_s^\star$ is the saturation humidity calculated from the underlying SST, u_s is the surface wind speed, u_0 is a constant background wind speed due to boundary layer turbulence, and K_p is a constant. The RH is assumed to be constant in x, but allowed to adjust to maintain energy balance, and c_p is chosen so that values of RH are reasonable. The addition of the $K_pP^{3/2}$ term is to capture the effects of "gustiness" associated with precipitation and mesoscale organizations that occur in the CRM. These wind gusts occur over length scales equal to or greater the grid (2 km) and are not captured in the time-mean surface winds. Since our simple model only searches for steady-state solutions, any transitory behavior must be parameterized. Capturing the effects of transients that influence the mean state, such as wind gusts in this case, is an important and nontrivial task in building steady-state simple models of complex time-dependent systems. A model parameterization for wind gusts in areas of precipitation was proposed by Redelsperger et al. (2000) and has been implemented in a SQTCM-like model in the past (Sugiyama 2009). However, our gustiness has a stronger dependence on P.

When the CRM's LHF (Fig. 7, blue) is approximated by the bulk scheme in Eq. (17) without gustiness, $K_p = 0$

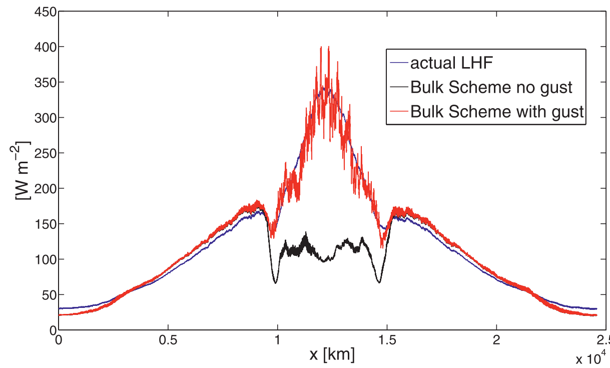

FIG. 7. The LHF from CRM (blue line), approximated with a bulk formula without (black line) and with gustiness (red line).

(black), the match is very good over the cold pool, but poor over the warm pool. When gustiness is applied, $K_p = 0.0022$ (red), the warm pool LHF is much better captured, making a compelling case for the inclusion of gustiness in the evaporation formula. It should be noted that for both the black and red curve, the RH used is the CRM's horizontally variant, low-level RH. In the simple model, we have chosen a value of K_p that is larger (2.5 times) than the value derived from the CRM in part to emphasize the role of the parameter, and also to compensate for error incurred by fixing relative humidity, since the CRM has a lower RH in the warm pool compared to the cold pool.

e. *Effective MSE stratification*

In PB05, M_q and M_s were based on horizontally uniform profiles and the difference between them, $M = M_s - M_q$ was the GMS, following the definition of Neelin and Held (1987). In our simple model, we have redefined M_q and M_s such that Eqs. (9) and (10) are straightforward when vertical velocity profiles are variable. This gives M_q the ability to capture different convective regimes (i.e., shallow, deep, strong, etc.). Here, we define a gross normalized effective MSE stratification (EMS):

$$\mathrm{EMS} = \frac{M_s - M_q}{M_s}. \qquad (18)$$

We refer to this as EMS and omit the term "gross normalized." EMS plays an important role in the energetics of the model as it links the column MSE sources to the strength of the divergent flow and advection. Here, we will compare our EMS to the GMS of PB05 and justify our modifications.

It is easy to show that for a fixed vertical structure $[V = V(p)]$, Eqs. (7) and (8) reduce to the PB05 definition. Beginning with the continuity equation

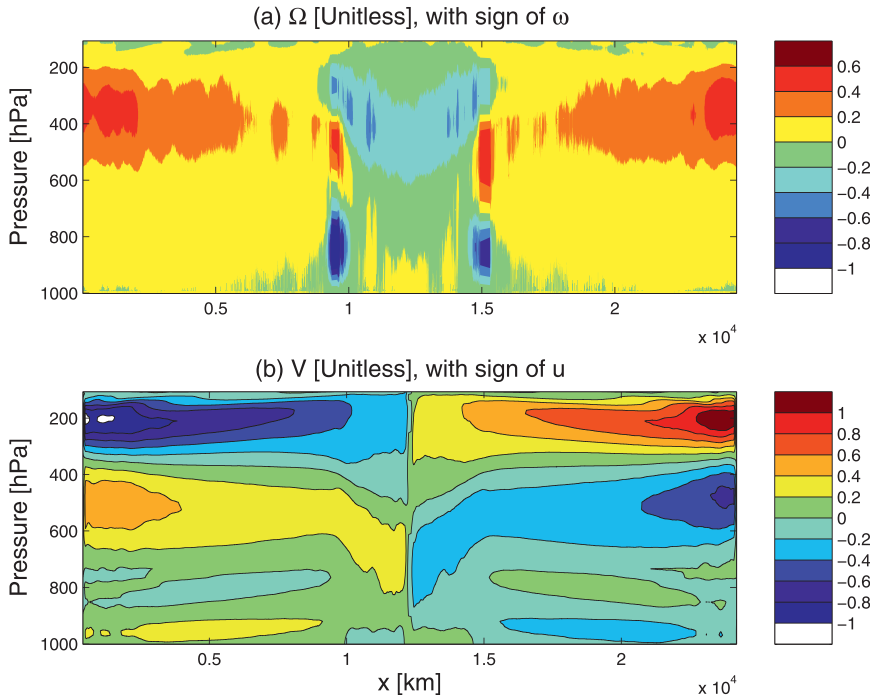

FIG. 8. The CRM control run values of (a) Ω multiplied by the sign of ω and (b) V multiplied by the sign of u. Positive values are for downward and rightward motions.

$$\frac{\partial}{\partial x}[V(p)u_1(x,t)] + \frac{\partial}{\partial p}[\Omega(p)\omega_1(x,t)] = 0,$$

combined with Eq. (6), we have

$$\frac{V(p)}{\Delta p_T} + \frac{\partial \Omega(p)}{\partial p} = 0.$$

Therefore,

$$\begin{aligned} M_q(x,t) &= \frac{1}{\Delta p_T}\int_{p_T}^{p_s} V(p)q(x,p,t)\,dp \\ &= -\int_{p_T}^{p_s} \frac{\partial \Omega(p)}{\partial p} q(x,p,t)\,dp = \int_{p_T}^{p_s} \Omega(p)\frac{\partial q(x,p,t)}{\partial p}\,dp, \end{aligned}$$

which is the M_q of PB05. In the last step, we performed integration by parts and used the rigid-lid upper and lower boundary conditions. The derivation of M_s follows the same steps.

We check the CRM velocity profiles by calculating Ω and V directly from the CRM. This is possible because of our demand that M_s be a uniform constant. They are computed by

$$V(x,p) = -\frac{M_s u(x,p)}{\dfrac{1}{\Delta p_T}\displaystyle\int_{p_T}^{p_s} u(x,p)s(x,p)\,dp}, \tag{19}$$

$$\Omega(x,p) = \frac{M_s \omega(x,p)}{\dfrac{1}{\Delta p_T}\displaystyle\int_{p_T}^{p_s} \omega(x,p)s(x,p)\,dp}. \tag{20}$$

Here V and Ω will be undefined where $u(p) = 0$ and $\omega(p) = 0$, respectively. For V, this occurs over the warmest and coldest SSTs, while for Ω it occurs at the warm pool–cold pool boundary. We plot both in Fig. 8, filtering near areas that are undefined by eliminating the 3% of points with the lowest denominators and smoothing in x by intervals of 500 and 200 km for Ω and V, respectively. As they are unitless, we choose to scale them such that the majority of points have an absolute value no greater than one. A noticeable feature in the Ω plot (Fig. 8a) is a transition from bottom to top-heavy vertical velocity profiles in the warm pool. Recent studies have similarly shown significant differences between vertical profiles in different locations of the Walker–Hadley circulation (Back and Bretherton 2006; Peters et al. 2008). The Ω profiles will affect u and V by continuity. Also, in trying to parameterize M_s and M_q from the CRM, the differences in profiles will affect the values. Note that V and Ω are used to diagnose M_s and M_q from the CRM and do not enter into the simple model in a significant way.

We examine M_q/M_s (or $1 - \text{EMS}$) from our results in the CRM as this quantity has easily understood values: when the atmosphere is dry, this ratio is equal to zero,

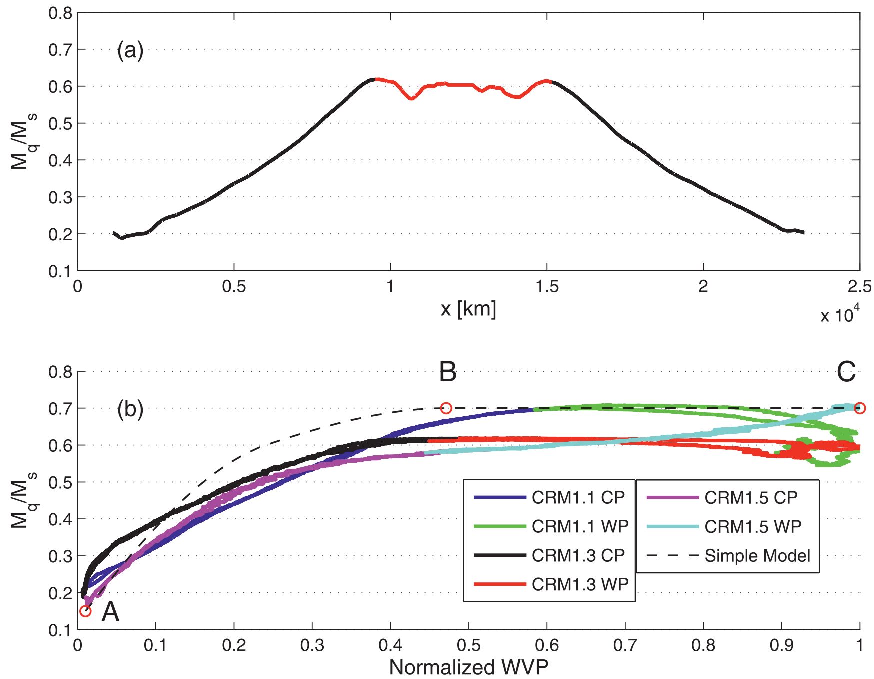

FIG. 9. The CRM M_q/M_s from various cases plotted against (a) x and (b) normalized free tropospheric WVP. Here, CP and WP indicate cold pool and warm pool; the legend applies to both (a) and (b), and the control run is denoted as CRM1.3.

and when the atmosphere has no MSE stratification, this ratio is equal to one. We plot M_q/M_s as a function of x for the CRM control case in Fig. 9a, filtering columns where the absolute value of the denominator in Eq. (19) is small, eliminating 10% of points, and smoothing over 600 km. Fixed M_s dictates that the changes seen in M_q/M_s are scaled changes in M_q. The positive trend in $\partial M_q/\partial$SST over the cold pool (Fig. 9a, black line) is easily understood as V (Fig. 8b) strengthens at lower levels (~900 hPa) and q increases at corresponding heights (Fig. 1d). The warm pool trend in $\partial M_q/\partial$SST (Fig. 9a, red line) is not as straightforward because of the competing effects between the boundary layer and the lower free troposphere: in the boundary layer (below ~800 mb), V decreases in strength and q decreases, having a negative effect on warm pool $\partial M_q/\partial$SST. In the lower free troposphere (~800 to ~500 mb), V strengthens and q strengthens, having a positive effect on warm pool $\partial M_q/\partial$SST. These two competing effects nearly cancel for the control case we have shown, resulting in a near flat trend, but in 1.1 K day^{-1} case, the trend is slightly negative, and in the 1.5 K day^{-1} case, the trend is slightly positive.

In trying to understand the warm pool trend in $\partial M_q/\partial$SST, we look at Ω (Fig. 8a), as these profiles show the different convective regimes operating. At the edge of the warm pool (x = ~9500 or ~15 000 km), a strong, shallow area of upward pressure velocity is present, likely due to dry horizontal advection lowering the humidity in the free troposphere, inhibiting convective updrafts from penetrating the upper troposphere (e.g., Brown and Zhang 1997; Parsons et al. 2000; Derbyshire et al. 2004; Kuang and Bretherton 2006; Peters et al. 2008). However, near the warmest SST, deep convection occurs and vertical velocity profiles have a first baroclinic mode structure. Profiles of V are broadly related to profiles of Ω through continuity (but not exactly). Thus, the V profiles from middle of the warm pool (x = ~10 500 km or ~13 000 km) have weaker winds at the lowest levels and develop a strong inflow between 500 and 800 mb. The moisture profile also changes from the edge of the warm pool to the middle of the warm pool, as the free troposphere moistens and lower levels dry, resulting in a drier column overall. While this phenomenon is not fully understood, there are natural analogs to this observed in convectively coupled waves (Straub and Kiladis 2002). Because of the variable forms of velocity profiles and their effect on the stratification, we allow horizontal variations in velocity profiles in the simple model, as previously detailed.

Our goal for the simple model is to be able to sort between different convective regimes seen in the CRM by prescribing M_q/M_s based on the CRM. To gain more resolution over the warm pool, we plot the CRM's M_q/M_s

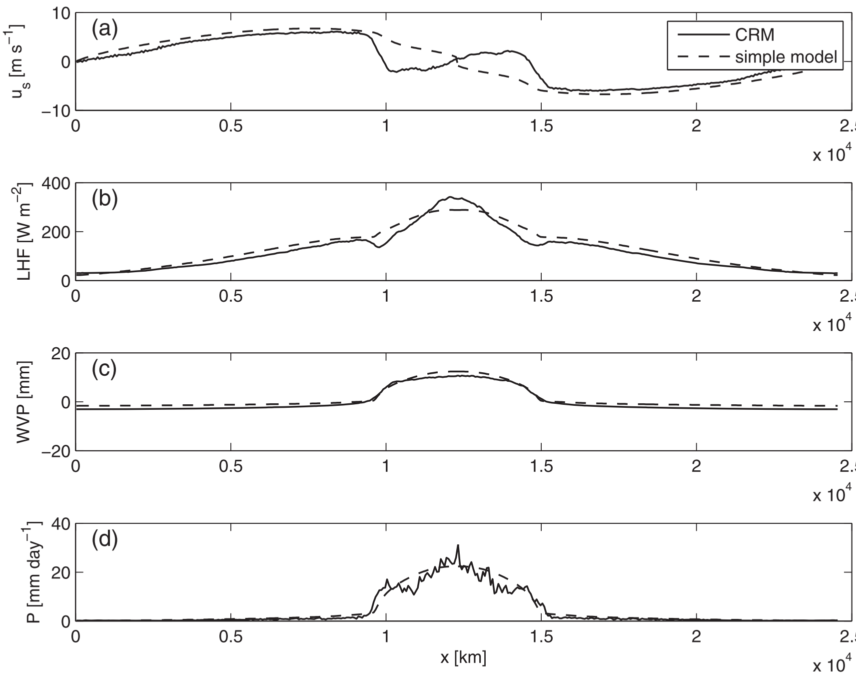

FIG. 10. Comparison of control runs between the CRM (solid) and the simple model (dashed) for (a) surface winds, (b) LHF, (c) WVP, and (d) precipitation.

as a function of WVP in the free troposphere (Fig. 9b), as this is a monotonic function of SST. Here, the differences in warm pool trends are magnified in the three separate cases. For our simple model parameterization, we perform a zero$^{\text{th}}$-order approximation passing through points A, B, and C (Fig. 9b), which have values of 0.15, 0.70, and 0.70, respectively. Point A is assigned to the lowest value of WVP, point B is assigned to the warm pool–cold pool boundary, and point C is assigned to the highest value of WVP. Interpolation between them is done with a shape-preserving piecewise cubic Hermite polynomial. This parameterization captures many of the salient components of the CRM, with a steady increase in M_q/M_s over the cold pool, quickly transitioning to a lesser slope over the warm pool. However, there are some differences between the simple model and the CRM cases. For instance, the simple model range is slightly greater than the range in the CRM cases. Also, the choice of the same value for B and C captures the near 0 slope of the 1.3 K day^{-1} over the warm pool, but the other cases have different slopes over the warm pool. Note that M_q/M_s is a major model control and we briefly discuss the sensitivity of the model to the choice of M_q/M_s in section 4c.

It should be noted that the assumptions made in our moisture equation, Eq. (3), enter the model enter in our prescribing M_q/M_s as a function of free tropospheric moisture, q_1. Also, M_q can vary in x since neither q_1 nor P is fixed in x.

4. Simple model results

a. Control results

A comparison between control runs of the simple model and the CRM shows good qualitative agreement when both models are run with the same SST gradient and radiative cooling rate. To approximate the column integrated radiative cooling rate in the CRM's 1.3 K day^{-1} cooling rate case, we use the domain average LHF (since sensible heat flux is small), which is 132 W m^{-2}. The simple model is initialized with radiative convective equilibrium as described in PB05, but model results do not depend on initial conditions. We then set R in Eqs. (9) and (11) to 132 W m^{-2} and solve for the rest of the variables. Figure 10 compares four fields for the control cases of the two models. A mirror image (about $x = A/2$; antisymmetric for winds) is included in all simple model results to make comparisons to the CRM easier. The surface winds, compared previously in Fig. 6, are presented again in Fig. 10a, showing very good agreement over the cold pool, with winds accelerating when moving toward the warm pool. In the warm pool, both models' winds decelerate, with the CRM's decelerating more rapidly. The good agreement heightens confidence in our hypothesis that the boundary layer momentum budget is the main control over surface winds in the CRM, although with an enhanced deceleration over the warm pool. Since there is little precipitation over the cold pool, the simple model cold pool winds will be similar in both an offline calculation and a full run, making it an a priori field if given the boundary layer structure. The surface winds will influence the LHF through the bulk formula in Eq. (17). Our hope is that by capturing the surface winds accurately in the simple model we will capture major features of the LHF accurately.

Comparing the LHF (Fig. 10b) of the two models, there are some qualitative similarities and some discrepancies. Both models show increasing LHF over the cold pool as winds increase. Both also show areas of wind gust–enhanced LHF over the warm pool despite weaker winds. However, the CRM has a local minimum in LHF on the edge of the warm pool and a stronger LHF peak that are not seen in the simple model. The CRM's increasing LHF over the warm pool is due to both gustiness and decreasing RH (not shown, but can easily be deduced from near-constant or decreasing low-level q over the warm pool seen in Fig. 1d). We try to account for this by increasing the gustiness factor in the simple model relative to value approximated from the CRM. A RH parameterization has been omitted to preserve the simplicity of the model.

The next field presented is the moisture field (Fig. 10c). Plotted is the CRM's free tropospheric water vapor path (above 2 km) with the mean value removed, and $\hat{b}q_1$ from the simple model. As $\hat{b}q_1$ is a perturbation from a background field, negative values are acceptable. Both models show a rapid increase in water vapor over the warm pool in response to the high LHF in the area and high M_q/M_s. In the simple model, τ_c was increased relative to PB05 to achieve a better match of this rapid increase.

We now turn our attention to the precipitation field (Fig. 10d). In the simple model, it is calculated with a Betts–Miller-like scheme presented in Eq. (12). Under WTG, T will be uniform in x, making the precipitation structure a function of moisture only. We hope that the good qualitative agreement in moisture fields will help to produce a qualitatively accurate precipitation field in the simple model. The CRM's precipitation rapidly increases at the edge of the warm pool where M_q/M_s is low and peaks over the warmest SST where deep atmospheric convection is present and free tropospheric WVP is highest. The simple model similarly shows a peak in precipitation over the warmest SST with a rapid increase in precipitation when moving from cold pool to warm pool. The rapid increase coincides with the point where M_q/M_s levels off and the peak coincides with the peak in free tropospheric moisture. However, there are differences between the models: the warm pool is slightly smaller in the simple model. Also, the CRM's curve has much more small-scale variability. In the CRM, precipitation is mesoscale and time dependent, wandering through the warm pool with convectively coupled waves as seen in a precipitation Hovmöller (Fig. 11). Moist convection can be shallow or deep and have a range of intensities. Given all of these complications, it is heartening that the simple model qualitatively captures the time-averaged CRM precipitation.

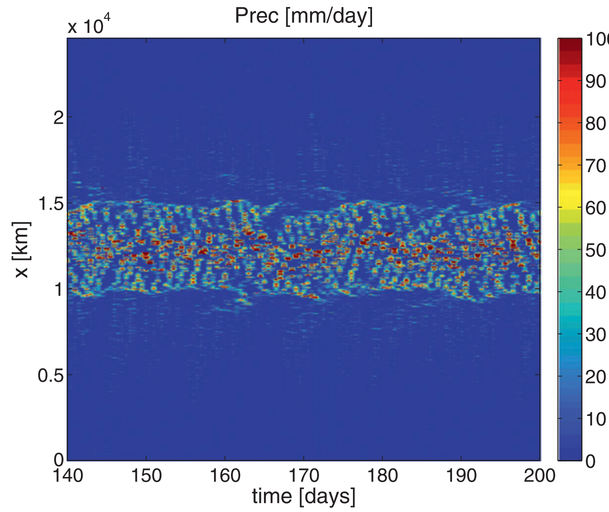

FIG. 11. The CRM control run precipitation Hovmöller diagram.

b. Behavior under variable radiative cooling rates

To further test the behavior of the simple model, we vary radiative cooling in a set of experiments similar to the set done with the CRM in section 2b. The increased radiative cooling case has a radiative cooling rate of 148 W m^{-2}, corresponding the average LHF of the 1.5 K day^{-1} CRM run. The decreased radiative cooling case has a radiative cooling rate of 113 W m^{-2}, the average LHF of the 1.1 K day^{-1} rate CRM run. The results of these experiments are presented in Fig. 12 for the same three fields shown for the CRM in Fig. 2.

The simple model surface winds (Fig. 12a) show little change with changing radiative cooling. They can only change through the precipitation feedback on drag, with almost no change seen outside of the warm pool. In contrast, the CRM's winds (Fig. 2a) do decrease slightly when radiative cooling is increased. The reason for this change is likely due to a small decrease in boundary layer slope. We have kept the boundary layer parameters the same for all calculations of the boundary layer winds to maintain simplicity. Since the boundary layer structure is not determined by the model, we have intentionally chosen cases in the CRM where the boundary layer structure does not vary greatly. This allows us to change radiative cooling without changing boundary layer parameters.

The simple model LHF curves (Fig. 12b) show an increase at all points when radiative cooling is increased.

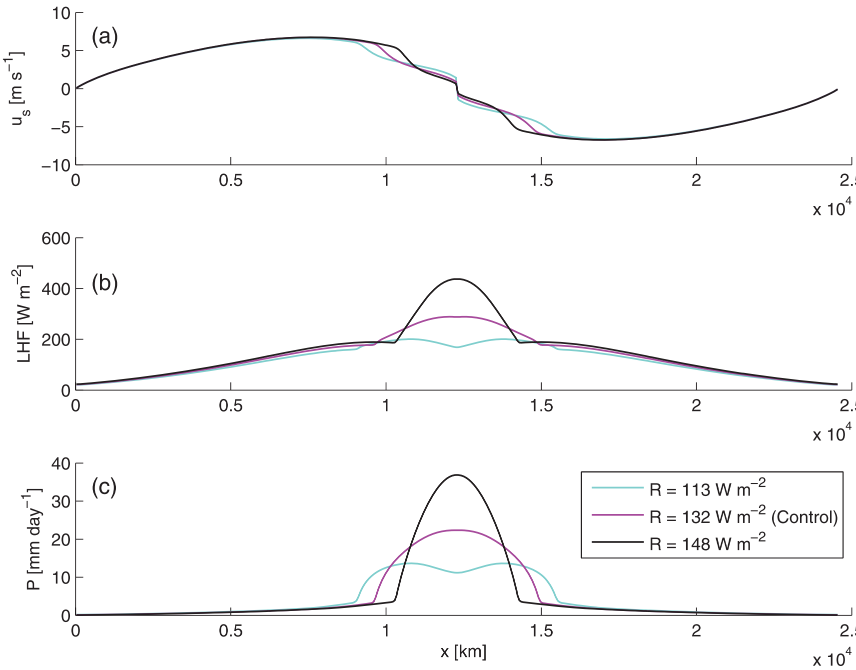

FIG. 12. Simple model results for different radiative cooling rates for (a) surface winds, (b) LHF, and (c) precipitation.

Domain averaged LHF will increase with higher radiative cooling; however, the increase is more pronounced over the warm pool. This is due largely to decreasing RH and the gustiness feedback, which is outlined in the next subsection. In the case of the CRM, there is a qualitatively similar increase in LHF (Fig. 2b), where the LHF increases over the warm pool almost exclusively. A notable difference between the models is that the CRM displays no increase or even slight decreases in LHF over the cold pool while the simple model has an increased LHF over the cold pool. This result is mainly due to the small changes in the CRM's surface winds, where the highest radiative cooling case (black) has the lowest surface winds.

The simple model precipitation curves (Fig. 12c) show a narrowing warm pool as radiative cooling is increased. The decreased radiative cooling case (cyan) shows a broad flat area of maximum precipitation, with a small local minimum over the warmest SST, while the increased radiative cooling case (black) has a much more peaked structure. When comparing against the CRM behavior (Fig. 2c), there is qualitative similarity in the narrowing trend of the warm pool and the more peaked shape of the increased radiative cooling case. While both the CRM and the simple model show similar overall changes in warm pool width, the CRM experiences most of this shrinking from the low radiative cooling to the control case, where it is more evenly spread distributed between the three cases in the simple model. The physical mechanism acting to narrow the warm pool is a feedback related to the gustiness parameter.

c. Gustiness feedback

In this section we illustrate how a gustiness feedback provides a physical mechanism for narrowing the warm pool in the simple model.

When gustiness in the simple model is turned off ($K_p = 0$), the warm pool does not narrow for any amount of radiative cooling increase (results not shown). Therefore, the narrowing mechanism must lie in the gustiness parameter, which enters the model through Eq. (17). To understand how this occurs, we come up with a procedure to approximate the rate of change in evaporation with respect to radiative cooling, $\partial E/\partial R$. Despite the simplicity of the model, a direct calculation of this quantity proves uninformative because of the coupling of multiple equations with various dependencies on R. We instead begin by assuming that the instantaneous response to raising the radiative cooling rate will be a drop in temperature. In a WTG framework, where temperature is uniform, this will cause a uniform rise in precipitation through Eq. (12). Without any change to RH, evaporation will then change if $K_p > 0$. Therefore, at this step we claim that

$$\frac{\partial E}{\partial R} = \frac{\partial E}{\partial P}. \quad (21)$$

From Eq. (17), $\partial E/\partial P$ takes the form of

$$\frac{\partial E}{\partial P} = \frac{C_1\sqrt{P}}{\sqrt{C_2 + K_p P^{3/2}}}, \tag{22}$$

where C_1 and C_2 are horizontally varying constants dependent on parameter choices and model conditions. We approximate Eq. (22) for the $R = 113$ W m^{-2} case by applying a uniform 1 W m^{-2} increase to the P field and putting that into Eq. (17) with no changes in winds or relative humidity and then remove the E field from the run. The result is shown in Fig. 13, where there is a disproportional increase in E over the warmest SST. The relative enhancement of evaporation over the warmest SST will lead to a relative increase in water vapor there compared to the surrounding area, which will then lead to more precipitation over the warmest SST, causing more E enhancement and creating a positive feedback loop. This will create a narrower warm pool, as P increases disproportionally more over the center of the domain. Other adjustments that occur will not have a disproportionate effect on fluxes and precipitation. For instance, relative humidity will fall to ensure $\overline{E} = \overline{R}$, but it is constant over the domain. The one exception is the precipitation enhanced drag K_{c_d}, which acts on the surface winds through a P dependence, and has a slight widening tendency on the warm pool. However, it is of negligible strength compared to the gustiness feedback.

It is apparent from the form of Eq. (22) that this feedback will saturate at high values of P. The choice of raising P to the 1.5 power in Eq. (17) was strong enough to demonstrate the effect of the gustiness feedback, but is somewhat uncertain. Attempts to quantify gustiness in a bulk formula have shown a saturation effect as well, but had a weaker dependence on P (Redelsperger et al. 2000). However, CRM experiments have shown a trend toward more gustiness enhancement of surface fluxes in areas of lower mean wind (Wu and Guimond 2006) and our warm pool has very low (down to 0 m s^{-1}) mean winds. Our formulation is meant to show the qualitative importance of gustiness on the evaporative budget and its control on warm pool width under variations in radiative cooling rate.

The existence of the gustiness feedback is very robust under variations in model parameters. We chose our model parameters with guidance from the CRM's output or observations if available. In the case of the precipitation-drag parameter K_{c_d} the newly defined M_q/M_s, diffusion, and the boundary layer wind, the inclusion is an effort to match the CRM control run result and because they add more realism to the model without adding too much

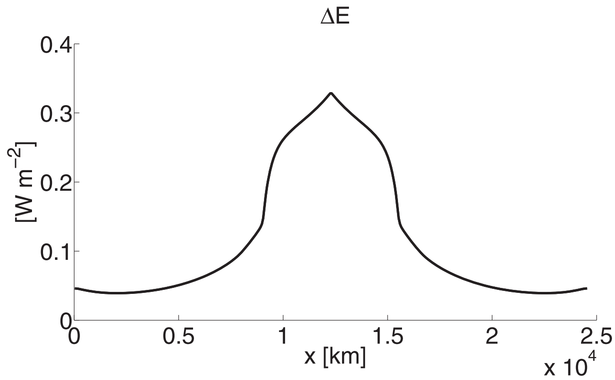

FIG. 13. Simple model change in evaporation in the 113 W m^{-2} case when precipitation is increased by a uniform 1 W m^{-2} and all other parameters are unchanged.

complexity. While changes to M_q/M_s in particular can lead to different control results, the narrowing effect of the gustiness feedback occurs in all of the wide range of cases we have tested. Also, narrowing occurs for all the strengths of the precipitation-drag feedback we have tried, from strong to none. Changing the control run result affects the sensitivity of the model since the gustiness feedback strength depends on P, but it does not change the qualitative behavior.

Using the postulated adjustment process leading to Eq. (21) of a uniform decrease in temperature as the first response to an increase in radiative cooling, aids interpretation of the PB05 result shown in Fig. 3. In this case, where there is no gustiness enhancement and no cold pool precipitation, a decrease in temperature without changing other variables will ultimately cause points outside of the precipitating region to reach the convective threshold, resulting in a wider region of precipitation.

Additional cases of more extreme forcings have been run in the CRM with interesting results (not shown) that could be investigated in future work. For instance, at very high rates of radiative cooling, the CRM's warm pool actually widens. This could be in response to a saturation of the gustiness feedback, as precipitation is very strong in these cases. However, these runs also involve other complex changes in the system that are not captured by the simple model.

5. Summary, discussion, and conclusions

We have presented results of a Walker simulation in a cloud-resolving model (CRM) run with fixed sea surface temperatures (SSTs) and fixed radiative cooling rates in the troposphere. The CRM was forced by changing radiative cooling rates. We observed a narrowing warm pool (area where $P > \overline{P}$) and preferential increase in latent heat flux (LHF) over the warmest SST when radiative cooling was increased. We created a simple model to explain and understand the behavior. The simple model was inspired by a previous simple model developed in PB05, but incorporated changes that we feel better captures the CRM. In particular, our model is now able to capture the narrowing warm pool seen in the CRM when radiative cooling is increased, which the model of PB05 was unable to reproduce. This was in response to a feedback created by LHF enhancement associated with wind gusts. Other changes made involved adding a surface wind parameterization, making LHF a function of wind speed, and horizontally varying vertical profiles of velocity.

To more accurately calculate the LHF, we calculated a surface wind by solving the boundary layer momentum equation. We then use the surface wind in calculating LHF. In PB05, the LHF was calculated without wind dependence. Since a major source of LHF variability is in the surface winds, we felt that this was an important addition to the model. The boundary layer momentum budget captures the winds over the cold pool (area where $P \leq \overline{P}$), but does not do as well over the warm pool, where deep atmospheric convection mixes momentum through a deep column. This phenomenon is parameterized by increasing the drag in proportion to the precipitation.

Some of our parameterizations could be the subject of future work. We have allowed for horizontal variability in vertical profiles of velocity and come up with a novel way to calculate the gross dry (M_q) and gross moist (M_s) stratification based on water vapor path and precipitation. However, we have prescribed the distribution. Since M_q/M_s is a major model control variable, developing a theory for how M_q/M_s evolves under different forcings would be useful in future work. Another way to further improve the accuracy of the simple model is to make a boundary layer model that interactively calculates boundary layer height and slope from model parameters, capturing more of the change in surface winds from case to case. Previous work on modeling the tropical boundary layer in a simple model (e.g., Kelly and Randall 2001) could provide guidance. Still another idea for improving the accuracy of the model is the addition of a surface relative humidity calculation to improve the accuracy of the LHF parameterization.

In addition to the wind dependence of LHF, we also add a gustiness dependence to capture the effect of transient wind gusts in the CRM. The ‘‘gustiness’’ captured by this parameter is bursts of wind, likely associated with mesoscale precipitation, not captured in the mean velocity field. The gustiness enhancement creates a feedback mechanism that narrows the warm pool when radiative cooling is decreased. It acts by disproportionally increasing the LHF over the warmest SST, which further increases the precipitation and creates a positive feedback.

It would be interesting to repeat these experiments with a mixed layer ocean instead of fixed SSTs. Increasing evaporation in the warm pool would either need to be balanced by high ocean heat transport, or the temperature of the water would drop. In experiments using a similar simple model, Bretherton and Sobel (2002) included a cloud radiative feedback in areas of precipitation which had a similar physical effect to our gustiness feedback. It was found that inclusion of a mixed layer ocean made changes in warm pool width less sensitive to the strength of the feedback (Sobel 2003; Sobel et al. 2004).

We have modified a simple model to better capture the Walker circulation behavior in a CRM in the absence of radiative feedbacks. In this process, we have generated a testable mechanism that can be explored in further simulations or observations. We plan to build upon this work and systematically add processes such as cloud radiative feedbacks and a mixed layer ocean to probe the complex interactions involved in the climatic responses to global warming.

Acknowledgments. Thank you to two peer reviewers for very helpful comments on a draft of this work. Additionally, the authors wish to thank Christopher Walker and the rest of the Harvard research computing staff for maintaining the Odyssey cluster that was used to run the CRM. We thank Joseph Fitzgerald for his insightful comments. We would also like to thank Matthew Peters for supplying the original model code. This research was partially supported by NSF Grants 19 ATM-0754332 and AGS-1062016. J. Wofsy wishes to thank the Harvard Earth and Planetary Sciences Department for funding in the initial phases.

APPENDIX

Boundary Layer Wind Solution

Begin with the hydrostatic balance in the boundary layer,

$$p_s(x) = \rho g H + \rho^+ g(D - H), \qquad \text{(A1)}$$

where D is the constant height of constant density above the boundary layer, $p_s(x)$ is surface pressure, ρ is boundary layer density, ρ^+ is the density above the boundary layer, g is gravity, and H is boundary layer height. The quantity

H increases when moving from the cold pool to the warm pool with the form

$$H = H_{\min} + m_b x, \tag{A2}$$

where $H_{\min}$ is the minimum boundary layer height and m_b is the boundary layer slope.

The pressure gradient in the boundary layer is

$$\frac{\partial p_s}{\partial x} = gH\left(\frac{\partial \rho}{\partial x} - \frac{\partial \rho^+}{\partial x}\right) + gD\frac{\partial \rho^+}{\partial x} + \frac{\partial H}{\partial x}g(\rho - \rho^+). \tag{A3}$$

Assuming that boundary layer temperatures closely follow the underlying SST, we have

$$T_b = T_0 - \Delta\mathrm{SST}\cos\left(\frac{2\pi x}{A}\right), \quad x \in \left[0, \frac{A}{2}\right], \tag{A4}$$

where $T_0 = \mathrm{SST}_0$. Approximating ρ as a perturbation from average boundary layer density ρ_0 we get

$$\rho(x) \approx \rho_0 + \frac{\rho_0}{T_0}\Delta\mathrm{SST}\cos\left(\frac{2\pi x}{A}\right) \tag{A5}$$

and

$$\frac{\partial \rho}{\partial x} \approx -\frac{\rho_0}{T_0}\frac{2\pi}{A}\Delta\mathrm{SST}\sin\left(\frac{2\pi x}{A}\right). \tag{A6}$$

If we assume $\partial\rho^+/\partial x \approx 0$ from WTG reasoning and

$$\rho_0 \gg \frac{\rho_0}{T_0}\Delta\mathrm{SST}\cos\left(\frac{2\pi x}{A}\right),$$

because $T_0 \gg \Delta\mathrm{SST}$, then substituting Eqs. (A5) and (A6) into Eq. (A3) yields

$$\frac{\partial p_s}{\partial x} = \frac{-gH\rho_0}{T_0}\frac{2\pi}{A}\Delta\mathrm{SST}\sin\left(\frac{2\pi x}{A}\right) + gm_b(\rho_0 - \rho^+). \tag{A7}$$

Now, consider the momentum balance:

$$u_b\frac{\partial u_b}{\partial x} = -\frac{1}{\rho_0}\frac{\partial p_s}{\partial x} - \frac{c_d}{H}u_b^2, \tag{A8}$$

where u_b is the boundary layer wind and c_d is the drag coefficient. Combine Eq. (A7) with Eq. (A8) and the assumption that the difference between ρ_0 and ρ^+ is small to finish with the following ODE for boundary layer wind:

$$\frac{1}{2}\frac{\partial u_b^2}{\partial x} = \frac{gH}{T_0}\frac{2\pi}{A}\Delta\mathrm{SST}\sin\left(\frac{2\pi x}{A}\right) - \frac{c_d}{H}u_b^2. \tag{A9}$$

Here, u_b is recalculated in the simple model with every adjustment of c_d. Equation (A9) is the same as Eq. (14).

REFERENCES

Arakawa, A., and W. Schubert, 1974: Interaction of a cumulus cloud ensemble with the large-scale environment, Part I. *J. Atmos. Sci.,* **31,** 674–701.

Back, L. E., and C. S. Bretherton, 2006: Geographic variability in the export of moist static energy and vertical motion profiles in the tropical Pacific. *Geophys. Res. Lett.,* **33,** L17810, doi:10.1029/2006GL026672.

Betts, A. K., and M. J. Miller, 1986: A new convective adjustment scheme. Part II: Single column tests using GATE wave, BOMEX, ATEX, and arctic air-mass data sets. *Quart. J. Roy. Meteor. Soc.,* **112,** 693–709.

Bony, S., and Coauthors, 2006: How well do we understand and evaluate climate change feedback processes? *J. Climate,* **19,** 3445–3482.

Bretherton, C. S., 2007: Challenges in numerical modeling of tropical circulations. *The Global Circulation of the Atmosphere,* T. Schneider and A. H. Sobel, Eds., Princeton University Press, 302–330.

——, and A. H. Sobel, 2002: A simple model of a convectively coupled Walker circulation using the weak temperature gradient approximation. *J. Climate,* **15,** 2907–2920.

——, P. N. Blossey, and M. E. Peters, 2006: Interpretation of simple and cloud-resolving simulations of moist convection–radiation interaction with a mock-Walker circulation. *Theor. Comput. Fluid Dyn.,* **20,** 421–442, doi:10.1007/s00162-006-0029-7.

Brown, R., and C. Zhang, 1997: Variability of midtropospheric moisture and its effect on cloud-top height distribution during TOGA COARE. *J. Atmos. Sci.,* **54,** 2760–2774.

Derbyshire, S., I. Beau, P. Bechtold, J. Grandpeix, J. Piriou, J. Redelsperger, and P. Soares, 2004: Sensitivity of moist convection to environmental humidity. *Quart. J. Roy. Meteor. Soc.,* **130,** 3055–3079.

Emanuel, K., J. Neelin, and C. Bretherton, 1994: On large-scale circulations in convecting atmospheres. *Quart. J. Roy. Meteor. Soc.,* **120,** 1111–1143.

Esbensen, S., and M. McPhaden, 1996: Enhancement of tropical ocean evaporation and sensible heat flux by atmospheric mesoscale systems. *J. Climate,* **9,** 2307–2325.

Grabowski, W. W., J. I. Yano, and M. W. Moncrieff, 2000: Cloud resolving modeling of tropical circulations driven by large-scale SST gradients. *J. Atmos. Sci.,* **57,** 2022–2039.

Holloway, C. E., and J. D. Neelin, 2009: Moisture vertical structure, column water vapor, and tropical deep convection. *J. Atmos. Sci.,* **66,** 1665–1683.

Jabouille, P., J. Redelsperger, and J. Lafore, 1996: Modification of surface fluxes by atmospheric convection in the TOGA COARE region. *Mon. Wea. Rev.,* **124,** 816–837.

Kelly, M., and D. Randall, 2001: A two-box model of a zonal atmospheric circulation in the tropics. *J. Climate,* **14,** 3944–3964.

Khairoutdinov, M., and D. Randall, 2003: Cloud resolving modeling of the ARM summer 1997 IOP: Model formulation, results, uncertainties, and sensitivities. *J. Atmos. Sci.,* **60,** 607–625.

Kuang, Z., and C. S. Bretherton, 2006: A mass-flux scheme view of a high-resolution simulation of a transition from shallow to deep cumulus convection. *J. Atmos. Sci.,* **63,** 1895–1909.

Larson, K., D. Hartmann, and S. Klein, 1999: The role of clouds, water vapor, circulation, and boundary layer structure in the sensitivity of the tropical climate. *J. Climate,* **12,** 2359–2374.

Lindzen, R., and S. Nigam, 1987: On the role of sea surface temperature gradients in forcing low-level winds and convergence in the tropics. *J. Atmos. Sci.,* **44,** 2418–2436.

Liu, C., and M. W. Moncrieff, 2008: Explicitly simulated tropical convection over idealized warm pools. *J. Geophys. Res.,* **113,** D21121, doi:10.1029/2008JD010206.

Mapes, B., and R. Houze, 1995: Diabatic divergence profiles in western Pacific mesoscale convective systems. *J. Atmos. Sci.,* **52,** 1807–1828.

Neelin, J. D., and I. M. Held, 1987: Modeling tropical convergence based on the moist static energy budget. *Mon. Wea. Rev.,* **115,** 3–12.

——, and N. Zeng, 2000: A quasi-equilibrium tropical circulation model: Formulation. *J. Atmos. Sci.,* **57,** 1741–1766.

Nuijens, L., and B. Stevens, 2012: The influence of wind speed on shallow marine cumulus convection. *J. Atmos. Sci.,* **69,** 168–184.

Parsons, D., K. Yoneyama, and J. Redelsperger, 2000: The evolution of the tropical western Pacific atmosphere–ocean system following the arrival of a dry intrusion. *Quart. J. Roy. Meteor. Soc.,* **126,** 517–548.

Pauluis, O., and S. Garner, 2006: Sensitivity of radiative–convective equilibrium simulations to horizontal resolution. *J. Atmos. Sci.,* **63,** 1910–1923.

Peters, M. E., and C. Bretherton, 2005: A simplified model of the Walker circulation with an interactive ocean mixed layer and cloud-radiative feedbacks. *J. Climate,* **18,** 4216–4234.

——, Z. Kuang, and C. C. Walker, 2008: Analysis of atmospheric energy transport in ERA-40 and implications for simple models of the mean tropical circulation. *J. Climate,* **21,** 5229–5241.

Pierrehumbert, R. T., 1995: Thermostats, radiator fins, and the local runaway greenhouse. *J. Atmos. Sci.,* **52,** 1784–1806.

Redelsperger, J., F. Guichard, and S. Mondon, 2000: A parameterization of mesoscale enhancement of surface fluxes for large-scale models. *J. Climate,* **13,** 402–421.

Sobel, A. H., 2003: On the coexistence of an evaporation minimum and precipitation maximum in the warm pool. *J. Climate,* **16,** 1003–1009.

——, and C. S. Bretherton, 2000: Modeling tropical precipitation in a single column. *J. Climate,* **13,** 4378–4392.

——, J. Nilsson, and L. M. Polvani, 2001: The weak temperature gradient approximation and balanced tropical moisture waves. *J. Atmos. Sci.,* **58,** 3650–3665.

——, C. S. Bretherton, H. Gildor, and M. E. Peters, 2004: Convection, cloud-radiative feedbacks, and thermodynamic ocean coupling in simple models of the Walker circulation. *Ocean–Atmosphere Interaction and Climate Variability, Geophys. Monogr.,* Amer. Geophys. Union, Vol. 147, 393–405.

Straub, K., and G. Kiladis, 2002: Observations of a convectively coupled Kelvin wave in the eastern Pacific ITCZ. *J. Atmos. Sci.,* **59,** 30–53.

Sugiyama, M., 2009: The moisture mode in the quasi-equilibrium tropical circulation model. Part II: Nonlinear behavior on an equatorial β plane. *J. Atmos. Sci.,* **66,** 1525–1542.

Wu, X., and S. Guimond, 2006: Two- and three-dimensional cloud-resolving model simulations of the mesoscale enhancement of surface heat fluxes by precipitating deep convection. *J. Climate,* **19,** 139–149.

Wyant, M. C., C. S. Bretherton, J. T. Bacmeister, J. T. Kiehl, I. M. Held, M. Zhao, S. A. Klein, and B. J. Soden, 2006: A comparison of low-latitude cloud properties and their response to climate change in three AGCMs sorted into regimes using mid-tropospheric vertical velocity. *Climate Dyn.,* **27,** 261–279.